Journal of
Manufacturing and Materials Processing

MDPI

Article

On Friction, Heat Input, and Material Flow Initiation during Friction Stir Welding: Tool and Process Optimization

Max Hossfeld †

Innovation Campus Future Mobility, University of Stuttgart, Nobelstraße 15, 70569 Stuttgart, Germany; max.hossfeld@ifsw.uni-stuttgart.de
† Former Affiliation: Materials Testing Institute, University of Stuttgart, 70569 Stuttgart, Germany.

Abstract: The Friction Stir Welding (FSW) process depends entirely upon mechanical contact between the tool and the workpiece. As a result of this, all process phenomena and process outcomes such as weld geometry and mechanical properties are governed by FSW's frictional system. The following work characterizes this system with a focus on process initialization, heat input and material flow. For this purpose, an experimental program for the isolated investigation of the frictional system was carried out. Short-term effects such as contact initiation, run-in behavior and frictional transitions are considered as well as the influences of process parameters and geometry. The system and its behavior are analyzed quantitatively and qualitatively by experiments altering the normal pressure, relative velocity, and tool geometry. The experiments demonstrate a self-similar behavior of the process, including an important wear transition which initiates the material flow, and a subsequent equilibrium of forces, heat balance, and temperatures. The interaction between the tool and the welded material is described, as is the link between the frictional interface and material flow initialization. Based on these findings, recommendations are provided for process optimization and tool design.

Keywords: friction stir welding; friction; contact; heat input; material flow; process optimization and tool design

Citation: Hossfeld, M. On Friction, Heat Input, and Material Flow Initiation during Friction Stir Welding: Tool and Process Optimization. *J. Manuf. Mater. Process.* **2023**, *7*, 34. https://doi.org/10.3390/jmmp7010034

Academic Editor: Enkhsaikhan Boldsaikhan

Received: 23 December 2022
Revised: 26 January 2023
Accepted: 28 January 2023
Published: 31 January 2023

1. Introduction

The Friction Stir Welding (FSW) process [1] depends entirely upon mechanical contact between the tool and the workpiece. As a result of this, all process phenomena and process outcomes such as weld geometry and mechanical properties are governed by FSW's frictional system. Despite this fundamental importance, the isolated investigation of the frictional system of the process is a comparably neglected research topic.

Various authors have emphasized the need for an adequate description of the mechanics of frictional heat generation in FSW since the very early days of research, e.g., for analytical [2–4] or numerical modeling [5–7]. However, it has often been noted that there would be a high experimental expenditure for an isolated and process-oriented characterization of the frictional system. *Schmidt and Hattel* emphasized the high complexity of the problem, with temperatures ranging from ambient to solidus temperatures, slip rates in the order of $1\,m\,s^{-1}$, and strain rates of up to $1000\,s^{-1}$, calling for a complex experimental setup [2]. The same authors stated that there may be few (if any) suitable laboratory procedures for replicating the friction system of FSW, and therefore recommended using the process itself. *Kumar et al.* underlined the high expenditure needed for frictional system characterization and the need for a simple experimental procedure that can reproduce the conditions of FSW [8]. Consequently, they proposed an approach for determining the (pseudo-coulomb) friction coefficient during FSW. To the best of the author's knowledge, this approach from *Kumar et al.* is still the only one which targets friction during FSW more generally and not related to a specific application, i.e., a welding case with specific parameters, joint and tool design. *Kumar et al.* studied the interaction of a simplified FSW

tool, a cylindrical steel pin with 7 mm diameter, and an AA 7020-T6 aluminum sheet with 4.4 mm thickness at three different contact pressures (13, 26, and 39 MPa), each combined with four different spindle speeds (200, 600, 1000, and 1400 rpm). With a duration of more than 30 min for each experiment and manual temperature recording every 30 s, the focus of their investigation was on the long-term behavior of the frictional system. Furthermore, due to its inertia, the experimental setup had only a limited capability to detect high-frequency force changes as they occur especially during the initiation phase. Using this approach, *Kumar et al.* found friction coefficients of 1.2–1.4 for conditions the authors described as similar to FSW (400–450 °C). This is significantly higher than the friction coefficients reported from calibrations based on welding experiments, which are usually on the order of 0.3 [5,9–11]. *Kumar et al.* also described a positive correlation of friction coefficient and temperature and a critical temperature for each contact pressure at which a steep increase in the coefficient was observed. This steep increase was attributed to sticking, and its critical temperature was found to decrease with increasing contact pressure.

Target of This Work

The target of this present work is to contribute to the understanding of FSW's frictional system and particularly the initialization of the welding process itself, including heat input and material flow. This work's focus is on the most common FSW application, the welding of aluminum alloys. In contrast to previous work, the experiments presented here focus on process-typical time scales, relative velocities and realistic tool dimensions. Transient effects during contact initiation, run-in behavior and frictional transitions are considered as well as influences of process parameters and geometry. Based on the results of the experiments, a detailed discussion of the interplay of tool and welded material, the local frictional conditions, and material flow initiation is presented. The work closes with a general discussion of FSW's frictional system with recommendations for tool and process design. Due to the scope of the experimental investigation, covering more than 130 single experiments, an open access data repository was created which includes supplementary material such as a video of the experiments (see [12]).

2. Experimental Setup and Procedure

For reproducing the physics of the FSW process, all the friction experiments were carried out on a dedicated FSW machine using real welding setups, i. e., anvil, fixtures but also tool and part material and dimensions, as shown in Figure 1. For applying the desired contact pressure during the experiments, the machine was run in force-control mode. For a better resolution of the forces, the machine was equipped with a telemetric system that measured torque, transverse and normal forces at approximately 1700 Hz. Only these values of the telemetry system were used for the calculations in this study. Tools were made from wear-resistant silver steel 1.2210 (115CrV3) hardened to 60 HRC, and were designed as thin-walled hollow cylinders, as shown in Figure 2. In this way, the interaction zone between the tool and the workpiece is completely covered directly after contact initiation (as in the industrial FSW process) and oxidation of the aluminum during the experiment is prevented. Furthermore, this design results in far more homogeneous relative velocities within the whole contact area compared to using cylindrical pins. A further advantage of using hollow cylinders is that debris layers can exit the contact zone more easily after being disrupted. This is an issue that *Kumar et al.* described in their work as being problematic when using cylindrical pins [8]. With diameters up to 16 mm, tool dimensions corresponded to real FSW tools capable of welding up to 10 mm deep (cf. [13]).

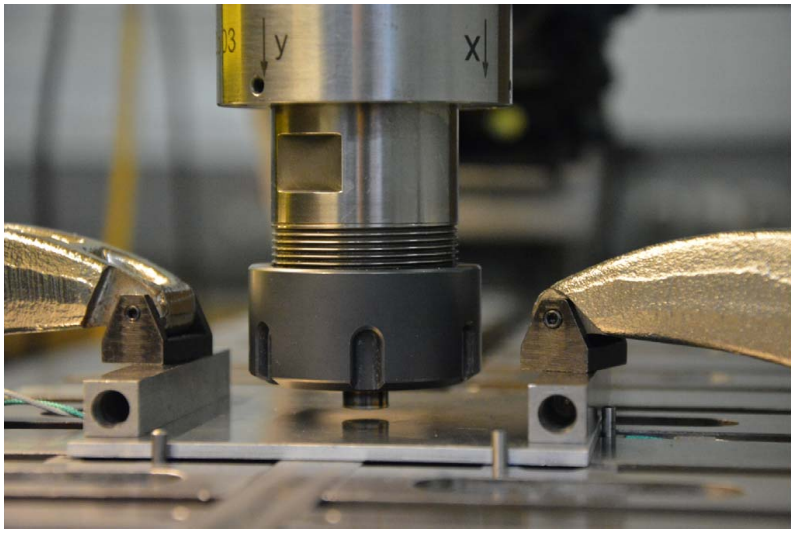

Figure 1. Experimental setup in starting position, with the telemetric system holding a tool (hollow cylinder), anvil, and fixtures.

The tool's frictional counterparts were aluminum sheets made from AA 5182-H111 (AlMg4.5Mn0.4). The material's exact chemical composition is provided in Table 1. AA 5182 is a non-hardenable aluminum alloy with comparatively good high-temperature strength, i.e., late thermal softening. Due to its relatively high deformability, AA 5182 is often used for structural components such as crash boxes and panels in vehicles. The material's temperature-dependent thermal and mechanical properties of are shown in Figure 3. As aluminum generally has a Pilling–Bedworth ratio [14] of 1.28, a very stable, dense and durable oxide layer forms on the alloy's surface. This layer typically has a thickness of 2–15 nm for Al–Mg alloys [15], and has a very high hardness (≈2000 HV 1) and high melting temperature (2072 °C). In order to provide a realistic heat sink, all sheets were 3 mm thick and 100 mm long and wide. For temperature measurement, all sheets were fitted with two Pt100 thermocouples positioned below the in middle of the contact area, as shown in Figure 2.

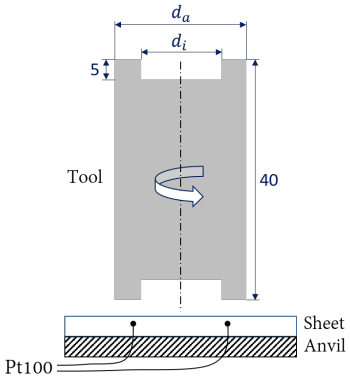

Tool	d_a	d_i
1	16	10
2	10	8
3	8	6
4	6	4
5	12	8
6	10	6
7	8	4
8	4	0

Figure 2. Schematic experimental setup with applied thermo-couples and tool dimensions of hollow cylinders.

Table 1. Chemical composition of the AA 5182 material used for this study as determined by spectral analysis (EDX).

Alloying Elements (wt%)										
Si	Fe	Cu	Mn	Mg	Cr	Zn	Ti	Ni	∑ other	Al
0.08	0.23	0.003	0.35	4.79	0.002	0.01	0.023	<0.001	<0.01	Rest

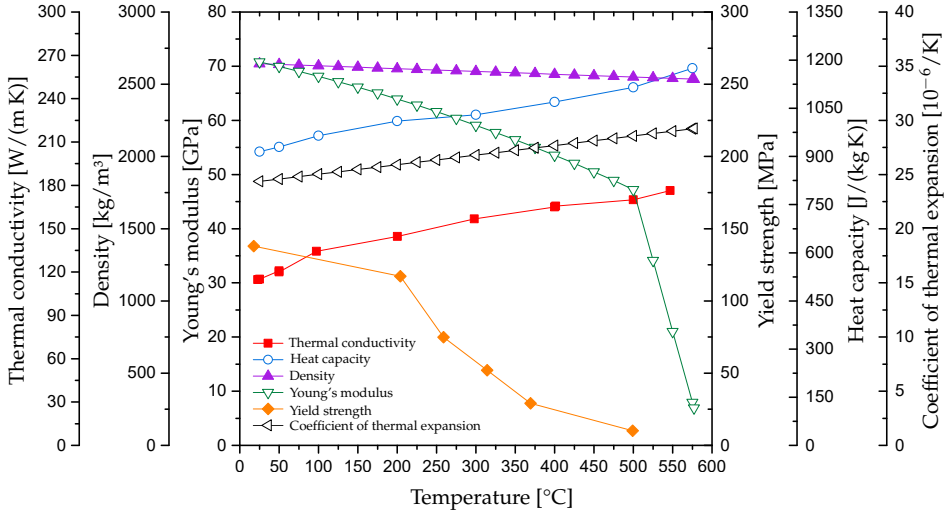

Figure 3. Temperature-dependent thermal and mechanical properties of AA 5182-H111; data from [4].

For each tool geometry, test series with fixed spindle speeds and increasing contact pressures were carried out. The initial contact pressure of each series was determined in advance on the basis of experiments without instrumentation. The procedure for each single experiment was as follows. With the tool mounted, the system was brought to the starting position as shown in Figure 1. After confirming that each component of the experimental setup had a temperature of 20 ± 2 °C, the spindle was started. After reaching the chosen spindle speed, the tool was brought into contact with the aluminum sheet. After a contact time of 20 s, the tool was retracted and the spindle was stopped. An example video of a friction experiment can be found in the related data repository of this publication; see [12].

3. Calculation of Shear Stress and Friction Coefficient from Measurements

The calculation of the friction coefficient was based on the measurements of the spindle torque M_t and normal force F_n, both of which were provided by the telemetric system. In order to take the geometric dimensions of the different tools into account, the effective shear stress in the contact area was calculated first, then substituted using Coulomb's definition.

In general, the following relationship exists between torque and the shear force distribution of any plane with an area A:

$$M_t = \int_A \tau(r) \cdot \pi r \, \mathrm{d}A \tag{1}$$

If this consideration is reduced to circular rings (as is valid for hollow cylinders), the substitution $\mathrm{d}A = 2\pi r \, \mathrm{d}r$ results in

$$M_t = \int_{r_i}^{r_a} \int_{\varphi=0}^{2\pi} \tau(r) \cdot r^2 \, \mathrm{d}\varphi \, \mathrm{d}r \tag{2}$$

where r_i and r_a are the inner and outer radii, respectively, and $\tau(r)$ is the shear stress distribution over the radius, as shown in Figure 4.

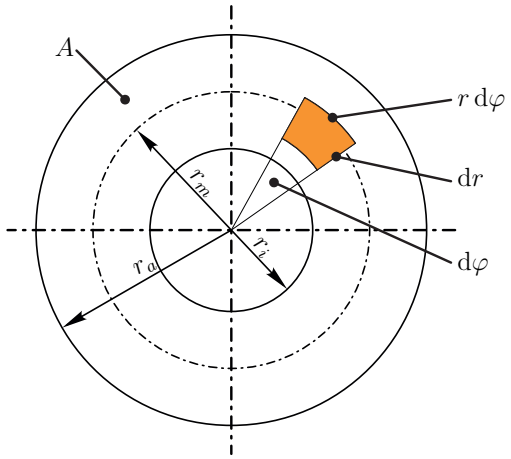

Figure 4. Schematic representation of the contact area of the hollow cylinder with the variables used for calculation.

Until the shear yield stress is reached, the shear stress τ_a at the outer radius is

$$\tau_a = \frac{M_t}{W_t} = \frac{M_t}{\frac{\pi}{16} \cdot \frac{d_a^4 - d_i^4}{d_a}} \tag{3}$$

and at the inner radius it is

$$\tau_i = \frac{M_t}{W_t} \cdot \frac{d_i}{d_a}. \tag{4}$$

Because we are interested in integral, average values for calculating the friction coefficient, an effective shear stress τ_{eff} is used in the following. However, without this being necessary for our further considerations, it could be argued as well that due to the thin walls of the tools and/or an ideal plastic material behavior after wear-in, the shear stress distribution in the contact area may be assumed to be approximately homogeneous. By using τ_{eff}, the equation for the resulting spindle torque can be obtained directly by integrating Equation (2):

$$M_t = \frac{2}{3} \tau_{\text{eff}} \pi \left(r_a^3 - r_i^3 \right) \tag{5}$$

where τ_{eff} can be substituted with $\mu\sigma_n$ according to Coulomb's definition:

$$M_t = \frac{2}{3} \mu\sigma_n \pi \left(r_a^3 - r_i^3 \right) \tag{6}$$

$$= \frac{2}{3} \mu \frac{F_n}{A} \pi \left(r_a^3 - r_i^3 \right) \tag{7}$$

$$= \frac{2}{3} \mu F_n \frac{r_a^3 - r_i^3}{r_a^2 - r_i^2} \tag{8}$$

In this way, μ can be determined on the basis of the quantities measured in the experiments. With this, the remaining variables result in

$$\mu = \frac{3M_t}{2F_n} \cdot \frac{r_a^2 - r_i^2}{r_a^3 - r_i^3} \tag{9}$$

$$r_m = \frac{2}{3} \frac{r_a^3 - r_i^3}{r_a^2 - r_i^2}, \quad F_R = \frac{M_t}{r_m}, \quad \tau_{\text{eff}} = \frac{F_R}{A}$$

4. Experimental Results

In accordance with the actual FSW process, a self-similar and self-stabilizing behavior was found throughout all the test series. This section initially provides a fundamental characterization of the frictional system based on one example test series. Afterwards, this characterization is extended to results from other test series, considering further influences and their effects, such as tool geometry or relative velocity. Based on these findings, an extended analysis of the local frictional conditions, the material behavior in the contact zone, and the induced material flow is provided.

4.1. Characterization of Frictional Behavior Based on Example Test Series

Directly after the initial contact between tool and workpiece, the frictional system is inevitably controlled by oxide or adsorption layers. These layers have to be broken up before metallic contact between the tool and substrate aluminum (and as such the FSW process itself) can be established. This change of the frictional system from being controlled by ambient oxides to being controlled by the metallic aluminum substrate represents a *friction transition* in tribology terms [16]. The transition includes wear processes such as breaking-in, running-in, or wearing-in.

Figure 5 shows an overview of the resulting surfaces and the course of friction coefficients and temperatures for an example test series. For this series, the inner and outer diameters of the tool were about 10 and 16 mm respectively. The exact wall thickness was between 3.07 mm and 3.14 mm, resulting in an area of 125.4 mm^2. The spindle speed during the experiments was set to 500 rpm, resulting in a relative velocity of about 350 mm/s. Table 2 summarizes the parameter sets of the test series.

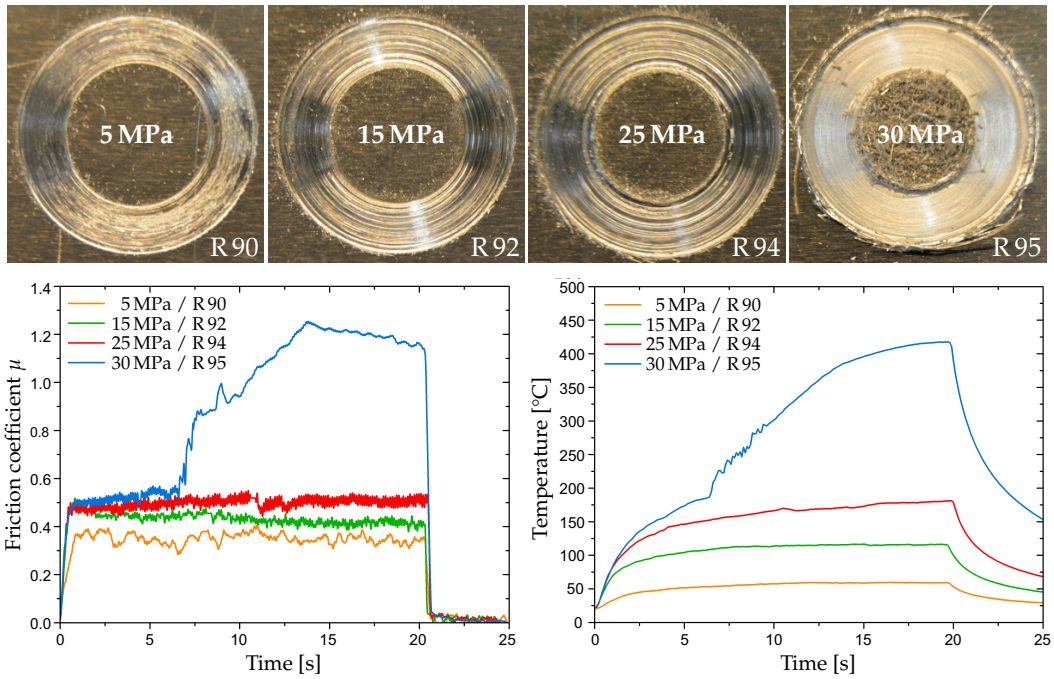

Figure 5. Surfaces, courses of friction coefficients, and temperatures for the example test series (Tool Number 1; spindle speed 500 rpm; different surface pressures; forces: moving average over 1 ms).

From the results of the surfaces shown, it can be seen that contact pressures up to 25 MPa essentially result in wear of the oxides only. Comparatively low contact pressures of 5 MPa (R 90) initially result in *abrasion* or *surface fatigue* wear mechanisms and the subsequent formation of a particle layer (debris) between the tool and workpiece.

With increasing contact pressure, this debris layer is pushed further into the sheet and the remaining oxides. This results in further abrasive mechanisms such as *micro-grooving* or *plowing*, cf. [16,17]. These can be identified by the circular grooves in the surfaces of the

samples R 92 and R 94 shown in Figure 5. With increasing contact pressure and as more and more oxide is broken up, the amount of debris exiting the contact area and accumulating around it increases as well.

Table 2. Parameter sets of test series R 90 to R 95 carried out with Tool Number 1 (as shown in Figure 2).

Exp.-No.	d_i [mm]	d_a [mm]	A [mm^2]	n [min^{-1}]	$v_{rel,m}$ [mm/s]	σ_n [MPa]
R 90	10	16	125.4	500	350	5
R 92	10	16	125.4	500	350	15
R 94	10	16	125.4	500	350	25
R 95	10	16	125.4	500	350	30

All of these processes are directly reflected in the resulting frictional forces. In general, the stochastic nature of the wear processes of the oxide results in localized microscopic impacts and vibrations which affect and interact with the frictional system and the machinery. This is particularly the case if the contact pressure is kept low and the contact between the workpiece and tool is barely initiated. The result is high scattering and unpredictable frictional forces. A typical example of this is the course of the friction coefficient μ for experiment R 90, which resulted in only a moderately worn surface (Figure 5). As the contact pressure is increased, the wear processes stabilize and micro-perturbations decrease. After this, the frictional forces increase almost linearly with the contact pressure. However, a slight increase in the friction coefficient with increasing contact pressure can be found when comparing R 92, R 94, and R 95. Overall, the oxide-controlled frictional system can be characterized by comparable low frictional forces, with friction coefficients μ typically ranging between 0.15 and 0.5. Corresponding to these low frictional forces, the heat input stays relatively low, e. g. for R 90 less than 90 W overall or 0.7 W/mm^2. Due to the high thermal conductivity of the substrate, a temperature equilibrium is reached quickly during the experiments. In this regime the resulting temperatures stay below 200°C and so do not cause a significant softening of the alloy, cf. Figure 3.

As the contact pressure is further increased, another wear mechanism evolves and becomes dominant. As temperatures reach the softening range of the AA 5182 alloy, the aluminum substrate starts to plastically deform below the oxide and the tool starts penetrating into the sheet. Since, compared to the base material, the oxide layer is very brittle, it cannot follow the aluminum's plastic deformation; therefore, it breaks up and is quickly dispersed. The removal of the oxide results in a direct metallic contact between the aluminum and the tool. As a result of the high local contact pressure and temperature [16], strong interfacial bonds are initiated, leading to an *adhesion* of the aluminum to the tool, cf. Figure 6. This is the beginning of the friction transition. Significantly higher tool forces are needed for dragging and shearing the adherent aluminum compared to the action of sliding over oxides. This results in self-reinforcing effects in two ways; first, the increase in frictional forces directly increases the heat input which further softens the aluminum locally; second, the strong plastic deformation of the aluminum being dragged with the tool efficiently breaks up and disperses any remaining oxides. The interplay of both effects results in rapid growth of the metallic contact area between the aluminum substrate and the tool, which in turn enhances both processes, i. e. a positive feedback loop is created.

In the case of R 95, this friction transition can be clearly recognized from the curve of the frictional coefficient, as shown in Figure 5. After about 6 s, the linear relationship of frictional and normal forces seen in the oxide-controlled experiments suddenly comes to an end. Almost instantaneously, the frictional coefficient doubles, followed by a further increase to about 250% of its initial value, as can be seen in Figure 5. To the same extent, the energy intensity increases from around 6 W/mm^2 to almost 15 W/mm^2, an increase from around 750 to 1750 W overall. With an effective shear stress in the contact zone of now almost 40 MPa, the heat generation is approximately twenty times higher than in

experiment R 90. Consequently, the temperature rises from about 200 °C to 425 °C. By the end of the transition, the frictional system is fully controlled by the behavior of the aluminum substrate. This situation has the following consequences: as the aluminum softens with increasing temperature, its resistance to mechanical deformation, and thus the heat input of the process, decreases. The result of this is an equilibrium of forces, heat balance, and temperature, which is well known from the actual FSW process. This interplay can be recognized in experiment R 95; about seven seconds after the transition (at 13 s overall) the friction coefficient starts to decline slightly, while the slope of the temperature rise flattens out. Due to this system behavior the heat input is self-limiting, resulting in asymptotic temperature curves not reaching the melting interval of the alloy. Figure 5 provides an overview of the surface of R 95 after the friction transition. Its white metallic shine clearly distinguishes it from the surfaces of R 90, R 92, and R 94, and strongly resembles the surface of real FSW seams. No remaining oxide layers can be identified within the former contact area. Moreover, the penetration of the tool into the aluminum sheet is clearly visible. Due to its geometry, the hollow cylindrical tool leaves a prominent elevation in the center that is covered by dispersed oxides. Figure 7 shows a barker-etched cross-section of sample R 95. In addition to the penetration of the tool into the sheet and the accumulation of oxides, another effect known from the actual FSW process can be recognized from the micro-structure; due to the severe plastic deformation of the material and the simultaneous heat impact, grain refinement is induced in the vicinity of the contact surfaces (continuous dynamic recrystallization—CDRX).

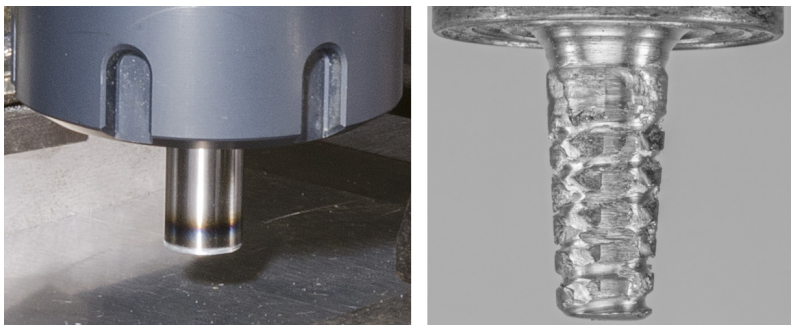

Figure 6. Aluminum adhering to tools after friction experiment (**left**) and real FS welding process (**right**).

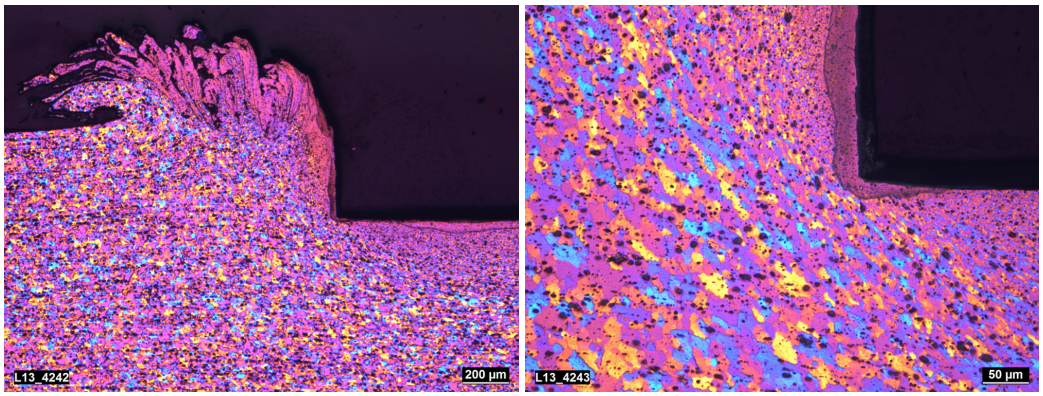

Figure 7. Cross-section of experiment R 95, showing wear-in, penetration, and continuous dynamic recrystallization. On the left: severe plastic deformation of the aluminum substrate and accumulation of oxides/former debris layers close to the contact.

The metal-controlled frictional system is clearly distinguished from the oxide-controlled one in several ways: first, by significantly higher friction coefficients with an associated higher heat input; second, by a material transfer of the aluminum to the tool surface due to high local temperatures and pressures; third, by being controlled by the material behavior

of the substrate, thus by a self-stabilizing behavior involving an equilibrium of forces, heat balance, and temperatures; and fourth, by the stabilization of the frictional system with the transition to being metal-controlled. This stabilization is reflected in the significantly lower scattering of frictional forces compared to the oxide-controlled frictional system. A short example video of a friction transition with the stabilization of the contact area is available in the data repository, along with unfiltered force diagrams showing the large degree of scattering; see [12].

4.2. Results from Further Test Series: Influences, Effects, and Correlations

Up to this point the focus of the characterization of the frictional system has concentrated on the behavior during the friction transition and the subsequent self-stabilizing phase. In the following section, this analysis is extended to cover two further aspects of the process: first, how the frictional system is influenced when geometrical boundary conditions are varied (contact area, relative velocity, etc.), and second, how the system behaves when the load is increased beyond the level needed for a frictional transition.

Table 3 provides an overview of the results of three tool geometries at different pressures and speeds. All combinations shown in the table achieved a friction transition. Images of all the surfaces involved are available in the data repository together with additional diagrams for experiments 2_{R045} to 2_{R069}. As stated before, all the experiments showed a similar behavior with the main differences being how quickly the wear transition was initiated and how long it took until an equilibrium of forces and temperature was reached (Figure 8).

Table 3. Overview of the results for three tool geometries at different pressures and speeds after the friction transition at the end of the respective experiment. Identifier Exp-ID w/ leading tool number, contact area A, spindle speed n, normal pressure σ_n, relative velocity $v_{rel,m}$, friction coefficient μ, effective shear stress τ_{eff}, and quasi-static temperature T_{stat}.

Exp-ID [+]	A [mm²]	n [min^{-1}]	σ_n [MPa]	$v_{rel,m}$ [mm/s]	μ [1]	τ_{eff} [MPa]	T_{stat} [°C]
1_{R095}	125.4	500	30	350	1.2	36	425
1_{R102}	125.4	1500	20	1020	0.45	9	305
2_{R045}	30.0	500	110	240	1.15	125	320 *
2_{R051}	30.0	750	65	350	1.17	76	270
2_{R052}	30.0	750	70	350	1.22	85	310
2_{R053}	30.0	750	75	350	1.18	88	325
2_{R030}	30.0	1000	55	470	0.99	55	220
2_{R060}	30.0	1500	50	710	0.74	37	355 *
2_{R063}	30.0	2000	25	940	0.80	20	330
2_{R069}	30.0	2000	45	940	0.82	37	425
6_{R005}	50.3	1000	40	420	0.83	34	300 *
6_{R006}	50.3	1000	50	420	0.78	38	310
6_{R010}	50.3	1500	25	630	0.92	23	290
6_{R013}	50.3	1500	40	630	0.68	27	350
6_{R016}	50.3	2000	20	840	0.65	13	260

[+] Leading digit: part number according to Figure 2; * at the end of experiment $\Delta T \not\approx 0$.

For experiment 1_{R102}, the same tool geometry was used as for the previous series. For direct comparison, experiment R 95 is included in the table with its tool number 1 as 1_{R095}. Both experiments are comparable since they were the first in their respective series, 500 and 1500 rpm, to achieve a wear transition. It can be clearly seen that at higher relative velocities, the friction transition can be achieved at a lower normal pressure. While at 500 rpm (350 mm/s) at least 30 MPa is needed, 20 MPa is sufficient at 1500 rpm (1020 mm/s). In comparison, experiment R 94 with a higher pressure of 25 MPa but a rotational velocity of only 500 rpm was not able to initiate a wear transfer and remained oxide controlled. Moreover, the higher rotational speed experiment 1_{R102} had a significantly lower effective

shear stress in the contact zone and a smaller friction coefficient after the wear transition compared to 1_{R095}. With an overall heat input of 1300 W, the temperature of 1_{R102} ranged around 305 °C at the end of the experiment, which is significantly below the temperature reached in the slower rotational speed sample 1_{R095} (1750 W/425 °C).

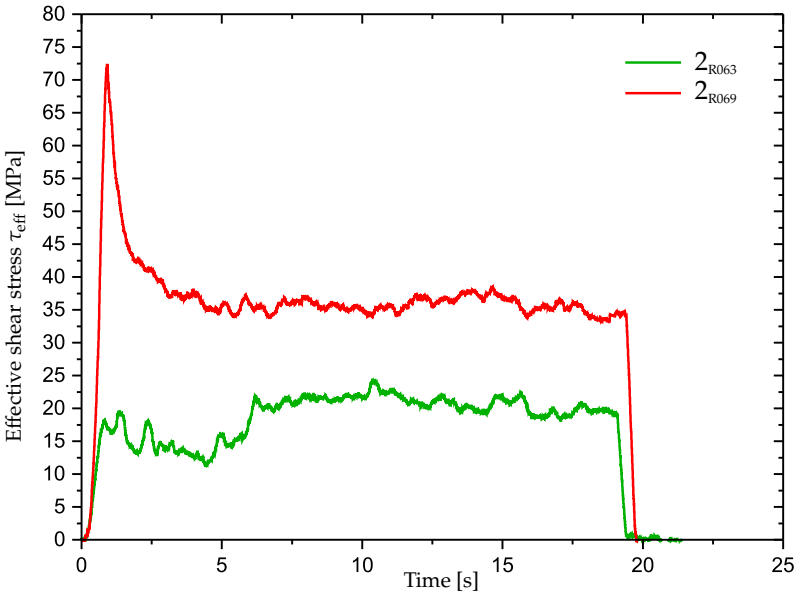

Figure 8. Effective shear stress during the wear transition of two experiments with 2000 rpm: 2_{R069} with 45 MPa, showing rapid transition almost instantaneously after contact; and 2_{R063} with 25 MPa, showing slower transition with a swing-in after about 5 s; both show subsequent stabilization of the system.

The findings of this direct comparison can be further generalized and extended by analyzing the results for tool geometries 2 and 6, shown in Table 3. With an outer diameter of 10 mm, both tools are significantly smaller than tool 1. Tool 2 has an inner diameter of 8 mm, i.e., a wall thickness of 1 mm and a contact area of 30.0 mm^2. Tool 6, with an inner diameter of 6 mm, has a wall thickness of 2 mm and a contact area of 50.3 mm^2.

From the results shown in Table 1, the following general relationships can be identified: after the friction transition, an increase of the normal pressure at the same relative velocity results in higher shear stresses and temperatures (cf. $2_{R051} - 2_{R052} - 2_{R053}$). As shown in these three experiments, the friction coefficient is not necessarily affected by this. Reduced friction coefficients are the result when the additional pressure causes the temperature to rise into the thermal softening range of the alloy, which in turn reduces its capacity for mechanical resistance (cf. 6_{R010} and 6_{R013}). However, the frictional coefficient reductions found during the experiments were always smaller than the relative increase in normal pressure; thus, the effective shear stress was increased. For example, when the normal pressure was increased by 60% from 25 to 40 MPa (6_{R010} to 6_{R013}), the friction coefficient decreased by about 25%. However, because the effective shear stress simultaneously increased by around 18%, the heat input rose to the same extent, from about 740 to 875 W. A finer gradation of this effect can be recognized when comparing experiments 6_{R005} and 6_{R006}. As with the normal pressure, increasing the relative velocity causes an increase in heat input, and thus the temperature. Simultaneously, there is a reduction of the effective shear stress. Increasing the relative velocity by 50% at 40 MPa from 420 to 630 mm/s (6_{R005} to 6_{R013}) results in a reduction of the effective shear stress from 34 to 27 MPa (−21%). The combination of both effects results in an increase of the heat input from 700 to 875 W (+24%) and a rise in the temperature from 300 to 350 °C.

Comparing the experiments, the sensitivity of the heat input to changing relative velocity or normal pressure is found to be comparable. Furthermore, it should be emphasized

that after the frictional transition, there is no linear relationship between a change in speed or contact pressure and the change in heat input. Again, the reason for this can found in the response of the material, i.e., the self-stabilizing behavior of the process. In analyzing the first experiments of each series achieving a friction transition, e.g., 2_{R030}, 2_{R045}, and 2_{R051}, a strong synergistic effect between contact pressure and velocity can be stated generally, with higher velocities requiring lower normal pressure to achieve a friction transition and vice versa.

Additional characteristics of FSW's frictional system can be identified by comparing results across tool geometries. For example, experiments 1_{R095} and 2_{R051} have the same relative velocity of 350 mm/s; nevertheless, more than twice the normal pressure of 1_{R095} was required to achieve a frictional transition in the case of 2_{R051}. The reason for this can be found in the more than 75% reduction in contact area and 67% reduction in wall thickness of tool 2. At 25 W/mm^2, the energy intensity for tool 2 is significantly higher than for tool 1 ($\approx$15 W/mm^2), while the overall heat input of 765 W is significantly lower (tool 1: 1750 W). This results in lower temperatures and a reduced softening of the alloy. Another example of the influence of tool geometry can be found in the comparison of experiment 1_{R095} with 2_{R069}. In both experiments, the same temperature was reached at the measuring location after 20 s. However, for generating the required heat input of 990 W, an intensity of 33 W/mm^2 was needed for tool 2. This is more than double the value required for tool 1. Generally, it has to be emphasized that despite the high variance of the input variables a comparatively homogeneous temperature range is found across the experimental series. In contrast to this, the friction coefficients show a large scatter, with an interval ranging from 0.45 to 1.22.

4.3. Extended Considerations, Multi-Layer Shearing, and Link to Material Flow

In the previous sections, the general character of FSW's frictional system and its influences has been clarified. One important characteristic aspect stands out as being of major importance, namely, transition of the system to being controlled by the aluminum adhering to the tool. This section addresses the reasons why such interfacial bonds form and then focuses on the implications for the FSW process.

In general, material transfer during frictional contact requires the formation of interfacial bonds, which have to be stronger than the inherent cohesion of the adhering material, i.e., its strength [18,19]. For such transfer and adhesion processes, the following relationships are known from the tribological literature:

- The adhesion tendency increases with decreasing hardness [20,21].
- The adhesion tendency increases depending on the lattice structure in the following order: *hcp-bcc-fcc* [17,22]. The reason for this is the different number of available slip planes, which influences the formation of the true contact surface.
- The adhesion strength increases in the following order: *transition metals-noble metals-metals of the boron group*, depending on their electron configuration and the associated possible bonding modes [18].
- The adhesion tendency increases with increasing contact temperature and with increasing contact pressure [16,17].

From this compilation, the high suitability of tool adhesion for materials commonly joined by FSW is obvious. Aluminum, for example, is typically FS welded at absolute temperatures of 0.6–0.8 T_S and normal pressures in the mid-two digit MPa range [4]. Aluminum has an fcc lattice structure and belongs to the boron group. In addition, with increasing temperatures, additional slip planes are activated in the material, further promoting the formation of interfacial bonds between the tool and workpiece. Moreover, it is clear from the above that the FSW tool material has to have a significantly higher hardness and strength than the processed material at processing temperatures.

As has been described on the basis of experiment R 95, the consequences of material adhering to the tool are extensive. Deeper material layers become involved in the development of the frictional contact when they are dragged along and deformed by the tool's movement, leading to *multi-layer shearing* [16] of the softer contact partner. As a

result, shearing and heat generation after the transition no longer takes place at the contact surfaces of the friction partners only, but also inside the workpiece itself, leading to a more diffuse heat input.

Figure 9 provides an example of how the FSW material flow around the tool is stimulated by multi-layer shearing; the figure shows a macro-level top view along the welding direction in the middle of a 3 mm deep weld. It can be seen that in front of the tool, even before making contact with the pin, the joint line is deflected by the material flow in the direction of rotation (white arrows). It is then entrained and drawn into the actual joining zone next to, or behind, the tool. During this process, a gradual mechanical disintegration of the oxides occurs. Parts of the original oxide layers may still be identified up to a rotation around the tool of about 270°. After this, no oxide fragments are visible (optical resolution ≈ 0.5 to 1.5 µm). In the example shown, a rotating cylinder forms that has a minimum extension in front of the tool of about 350 µm. This corresponds to an increase in the effective area of the tool of about 15%. Behind the tool, an expansion of slightly more than 500 µm (almost 25%) is achieved.

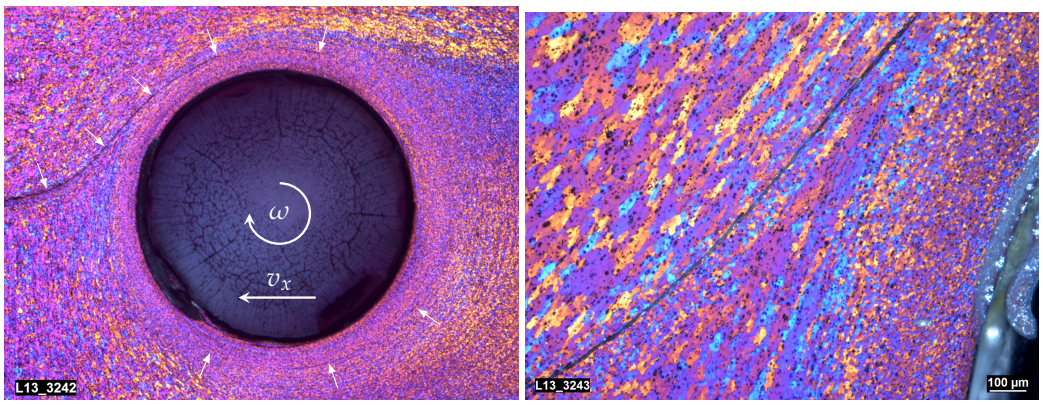

Figure 9. Co-rotating material flow around and initial deformation zone in front of the tool. Oxides of the former joint line are dragged into the joining zone and mechanically disintegrated (white arrows). The top view shows the middle of a 3 mm deep FS weld macro-section along the welding direction.

Adhesion and multi-layer shearing provide an explanation for the lifetime of FSW tools as well. In well-adjusted FSW applications, tools may last up to a few kilometers of weld seam length in aluminum. But even if a usable distance of only 500 m and a welding speed of 2 m/min are considered, this means a contact time between tool and workpieces of more than 4 h. Especially for tools with detailed active material flow structures, such lifetimes could not be possible for steady contact of the tool material with the very hard aluminum oxides under FSW conditions. This point is supported by the fact that when the contact between tool and oxide is enforced, e.g., by welding oxide-reinforced aluminum alloys [23,24], tools wear out rapidly and fail after a few meters. The reason for the comparatively low wear of FSW tools is explained by the co-rotating material flow, which prevents contact with oxides and so protects the tool and its geometrical structures.

5. Discussion of Results and Recommendations for Process and Tool Design

In the following section, the major findings of this work and their general implications for the state-of-the-art in scientific and industrial FSW applications are discussed.

First, it can be stated that during the friction stir welding process, fundamentally different friction regimes are present at different locations of the tool at the same time, depending on whether or not there is a (transient) adhesion of material to the tool [25]. In some parts of the contact area of the shoulder, the constant feed of oxides during traversing results in a dry, Coulombian friction on the workpiece surface oxide. By contrast, such frictional conditions can be virtually excluded outside the shoulder area due to the adhesion of material to the tool. The exact ratios and extents of these regimes depend on the individual application details, e.g., tilt angle, shoulder diameter, welding depth,

traverse speed, etc. The simultaneous presence of the different friction regimes may explain why analytical and numerical back-calculations from experiments usually yield apparent global friction coefficients of about 0.3, while friction experiments of this study and also the work of *Kumar et al.* [8] show significantly lower values before the friction transition and significantly higher values afterwards in comparable cases.

In this context, it can be assumed that the shoulder is generally responsible for the largest share of the normal forces due to its contact area. However, due to the very different friction conditions at the shoulder and pin, the widespread view that the shoulder generates the vast majority of the heat input [26,27] has to be reconsidered. This point is supported by the fact that FS welding is possible with very small shoulders [28] and even without shoulders [13]. Directly related to this finding is the consequence for analytical and numerical process modeling that the use of constant, global friction coefficients is only useful to a very limited extent.

Recommendations for Process and Tool Design

Based on these experiments, specific recommendations for the process and tool design of FSW can be given. While experiment 2_{R069}, with a high relative velocity and a high normal pressure, almost instantly achieved a wear transition (Figure 8), it took 1_{R095} about 7 s to initiate it (Figure 5). During this initiation phase, the tool is heavily exposed to the hard and abrasive aluminum oxides. Prolonged initiation is unnecessary for the welding process, and promotes tool wear. Therefore, the target of process and tool design should be to minimize the tool–oxide contact time. In light of this, the following approaches are recommended:

First, process initialization needs to be completed as quickly as possible. In the experiments, high contact pressures and high relative velocities ensured rapid initiation, i.e., the oxides were quickly dispersed or displaced from the contact zone, the material was rapidly softened, and the equilibrium state was reached quickly. In particular, high rotational speeds can be recommended here, at least during the penetration phase, as they result in a lower mechanical load on the tool compared to increasing the normal pressure. In this context, a slim, conical pin geometry is recommended for rapid penetration. In addition, faster process initialization can be achieved by using an aggressive contour to mechanically disrupt the oxide layers, thereby exposing the metal substrate. Figure 10 shows an example of this type of tool design.

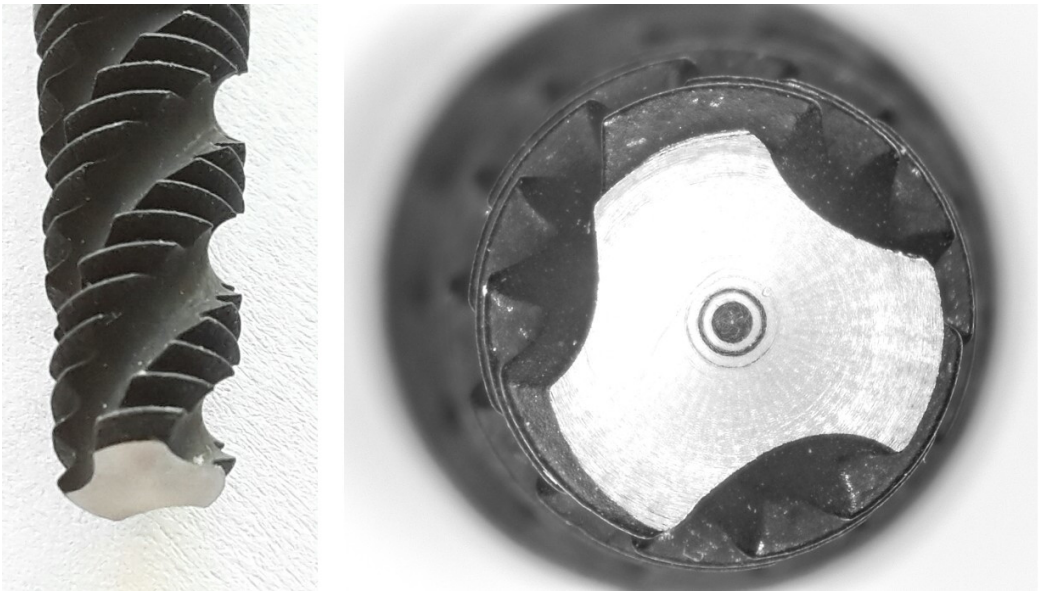

Figure 10. Example tool geometry optimized for fast process initiation and deep plunging, as used and evaluated in [13].

Second, in order to minimize the contact of the tool with oxides during the post-initiation welding process, i.e., traversing, tools with the smallest possible shoulder diameters should be used. This can greatly reduce the overall oxide contact of the process, as the shoulder is usually the largest oxide-contacting area of the tool. In order to achieve the same welding performance, higher spindle speeds and feed rates can be used for such narrower tools. This increases the process efficiency, as the total heat input and volume of processed material are reduced. For reducing the contact with oxides in the pin area, the adhesion of the material to the tool should be actively encouraged. This can be done, for example, by tool designs which encourage a strong material flow around the tool; moreover, aggressive tool features can be applied to soften the material around the tool locally via extensive shearing [13].

FSW equipment could benefit from the above-mentioned approaches in two ways: through significant reduction of shock-like excitation, and through reduction of the reaction forces imposed on smaller tools. From a process engineering point of view, this can improve the performance of existing FSW machines, e.g., by increasing the possible welding depths or speeds. There is also the possible benefit of the integration of FSW in systems which are less stiff and robust, such as milling machines. At the same time, a reduction in the oxide feed to the joining zone by minimizing joint line remnants (JLRs) can improve the mechanical properties of the weld as well as the process stability.

Further opportunities for optimization of the process and tool design result from the interchangeability of relative velocity and normal force found in the experiments. For existing tooling, this provides the possibility of regulating the heat input via the normal force instead of the spindle speed (which is the standard procedure in industry today). In the case of heavily contoured tools or narrow process envelopes, this can have the major advantage of influencing the material flow considerably less than altering the spindle speed.

6. Conclusions

The target of this work was to contribute to the knowledge about FSW's frictional system. A method for the experimental examination of this system was proposed, and an experimental program for the isolated investigation of the frictional system was carried out.

Based on the experimental results, the frictional system and its transition during the FSW process from being oxide-controlled to being metal-controlled was analyzed. During the initiation phase, the oxide-controlled frictional system can be characterized by comparatively low frictional forces, with friction coefficients μ typically ranging between 0.15 and 0.5 and a correspondingly low heat input.

After tool penetration, the metal-controlled frictional system is clearly distinguished by significantly higher friction coefficients up to 1.4 and correspondingly higher heat input. Due to high local temperatures and pressures, material transfer of the aluminum to the tool surface is initiated. After this, the frictional system is dominated by the behavior of the aluminum and thus shows a self-stabilizing behavior involving an equilibrium of forces, heat balance and temperatures.

The adhesion of material to the tool induces *multi-layer shearing* of the softer contact partner (aluminum), which stimulates a co-rotating material flow. Based on real welding conditions, the effect of *multi-layer shearing* was quantified and its impact on the material flow, heat input, and mechanical disintegration of oxides was described. Moreover, the importance of adhesion for the service life of FSW tools was emphasized.

Based on the findings, a number of recommendations for process optimization and tool design were provided. These advocate, among other things, slim tools with small shoulders, strong material flow structures, and rapid process initialization. The active utilization of the adhesion of material to the tool is recommended to minimize contact with the hard abrasive oxides.

The strategies presented for the reduction of process forces enable more efficient processes as well as the implementation of FSW on smaller machines, and as such offer opportunities for process integration, e.g., in milling operations.

This work provides a basis for future investigations of many further contact-related topics in FSW. In the author's view, the most important aspect is the influence of material adhesion on the material flow, especially with regard to the effectiveness and design of active material flow structures and their minimum effective size. Other important topics include the influence of the tool material and coatings on the frictional system, which is directly related the heat distribution between the tool and the workpiece.

Funding: Parts of this work, specifically, the friction experiments, were supported by the German Research Foundation (DFG) Project RO 651/16-1, which is greatly appreciated.

Institutional Review Board Statement: Not applicable.

Informed Consent Statement: Not applicable.

Data Availability Statement: Supplementary material are provided via a data repository; see [12]. Further micro-sections, machine logs, and videos are available from the author upon request.

Acknowledgments: The author wants to thank Rudi Scheck, Volkher Onuseit, and John Powell for supporting this work. Rudi Scheck from the MPA Stuttgart skillfully prepared the Barker etched cross-sections. Volkher Onuseit supported this publication via tactical coffee breaks. With his wise comments, John Powell greatly improved the readability and stringency of the paper.

Conflicts of Interest: The author declares no conflict of interest.

Nomenclature/Variables

Variable	Unit	Name
A	mm²	(Contact) Area
d_a	mm	Outer diameter
d_i	mm	Inner diameter
r_a	mm	Outer radius
r_i	mm	Inner radius
r_m	mm	Effective radius / lever
n	min^{-1}	Spindle speed
$v_{\mathrm{rel,m}}$	mm/s	Relative velocity
F_n	N	Normal force
M_t	Nm	Torque
T_{stat}	°C	Quasi-static Temperature
τ	MPa	Shear stress
μ	1	Friction coefficient
σ_n	MPa	Normal pressure

References

1. Thomas, W.; Nicholas, E.; Needham, J.; Murch, M.; Temple-Smith, P.; Dawes, C. Improvements Relating to Friction Welding. GB Patent No. 9125978-8, 6 December 1991.
2. Schmidt, H.B.; Hattel, J.H. Thermal modelling of friction stir welding. *Scr. Mater.* **2008**, *58*, 332–337. [CrossRef]
3. Colligan, K.J.; Mishra, R.S. A conceptual model for the process variables related to heat generation in friction stir welding of aluminum. *Scr. Mater.* **2008**, *58*, 327–331. [CrossRef]
4. Hoßfeld, M. *Experimental, Analytical and Numerical Investigations of the Friction Stir Welding Process*; Universität Stuttgart: Stuttgart, Germany, 2016. [CrossRef]
5. Assidi, M.; Fourment, L.; Guerdoux, S.; Nelson, T.W. Friction model for friction stir welding process simulation: Calibrations from welding experiments. *Int. J. Mach. Tools Manuf.* **2010**, *50*, 143–155. [CrossRef]
6. Dialami, N.; Chiumenti, M.; Cervera, M.; Segatori, A.; Osikowicz, W. Enhanced friction model for Friction Stir Welding (FSW) analysis: Simulation and experimental validation. *Int. J. Mech. Sci.* **2017**, *133*, 555–567. [CrossRef]
7. Liu, Q.; Li, W.; Zhu, L.; Gao, Y.; Xing, L.; Duan, Y.; Ke, L. Temperature-dependent friction coefficient and its effect on modeling friction stir welding for aluminum alloys. *J. Manuf. Process.* **2022**, *84*, 1054–1063. [CrossRef]
8. Kumar, K.; Kalyan, C.; Kailas, S.V.; Srivatsan, T.S. An Investigation of Friction During Friction Stir Welding of Metallic Materials. *Mater. Manuf. Process.* **2009**, *24*, 438–445. [CrossRef]
9. Chao, Y.J.; Qi, X. Thermal and thermo-mechanical modeling of friction stir welding of aluminum alloy 6061-T6. *J. Mater. Process. Manuf. Sci.* **1998**, *7*, 215–233. [CrossRef]

10. Guerdoux, S.; Fourment, L. A 3D numerical simulation of different phases of friction stir welding. *Model. Simul. Mater. Sci. Eng.* **2009**, *17*, 075001. [CrossRef]
11. Hossfeld, M.; Roos, E. A new approach to modelling friction stir welding using the CEL method. *Adv. Manuf. Eng. Technol.* **2013**, *2*, 179–190. [CrossRef]
12. Hoßfeld, M. *Supplementary Data for Paper "On Friction, Heat Input and Material Flow Initiation During Friction Stir Welding: Tool and Process Optimization"*; DaRUS: Stuttgart, Germany, 2023. [CrossRef]
13. Hossfeld, M. Shoulderless Friction Stir Welding: A low-force solid state keyhole joining technique for deep welding of labile structures. *Prod. Eng.* **2022**, *16*, 398–399. [CrossRef]
14. Bedworth, R.E.; Pilling, N.B. The oxidation of metals at high temperatures. *J. Inst. Met.* **1923**, *29*, 529–582.
15. Wakefield, G.R.; Sharp, R.M. The composition of oxides formed on Al-Mg alloys. *Appl. Surf. Sci.* **1991**, *51*, 95–102. [CrossRef]
16. Blau, P.J. *Friction Science and Technology: From Concepts to Applications*, 2nd ed.; CRC Press: Boca Raton, FA, USA, 2009.
17. Rabinowicz, E. *Friction and Wear of Materials*, 2nd ed.; A Wiley-Interscience Publication; Wiley: New York, NY, USA, 1995.
18. Czichos, H.; Habig, K.H. *Tribologie-Handbuch: Tribometrie, Tribomaterialien, Tribotechnik*; Mit 123 Tabellen Studium; Vieweg + Teubner: Wiesbaden, Germany, 2010.
19. Duffin, F.D.; Bahrani, A.S. Frictional behaviour of mild steel in friction welding. *Wear* **1973**, *26*, 53–74. [CrossRef]
20. Sikorski, M.E. Correlation of the Coefficient of Adhesion With Various Physical and Mechanical Properties of Metals. *J. Basic Eng.* **1963**, *85*, 279. [CrossRef]
21. Sikorski, M.E. The adhesion of metals and factors that influence it. *Wear* **1964**, *7*, 144–162. [CrossRef]
22. Buckley, D.H. The Influence of the Atomic Nature of Crystalline Materials on Friction. *ASLE Trans.* **1968**, *11*, 89–100. [CrossRef]
23. Prado, R.A.; Murr, L.E.; Soto, K.F.; McClure, J.C. Self-optimization in tool wear for friction-stir welding of Al 6061+20% Al2O3 MMC. *Mater. Sci. Eng. A* **2003**, *349*, 156–165. [CrossRef]
24. Santella, M.; Grant, G.; Arbegast, W. Plunge Testing to Evaluate Tool Materials for Friction Stir Welding of 6061 + 20 wt%Al2O3 Composite. In Proceedings of the 4th International Friction Stir Welding Symposium, Park City, UT, USA, 14–16 May 2003.
25. Schmidt, H.; Hattel, J.; Wert, J. An analytical model for the heat generation in friction stir welding. *Model. Simul. Mater. Sci. Eng.* **2004**, *12*, 143–157. [CrossRef]
26. Reza-E-Rabby, M.; Tang, W.; Reynolds, A. Effect of Tool Pin Features and Geometries on Quality of Weld During Friction Stir Welding. In *Friction Stir Welding and Processing VII*; Mishra, R., Mahoney, M.W., Sato, Y., Hovanski, Y., Verma, R., Eds.; Springer International Publishing: Cham, Switzerland, 2016; pp. 163–171. [CrossRef]
27. Pew, J.W.; Nelson, T.W.; Sorensen, C.D. Torque based weld power model for friction stir welding. *Sci. Technol. Weld. Join.* **2007**, *12*, 341–347. [CrossRef]
28. Mahoney, M. Learning from the Past. In Proceedings of the 12th International Friction Stir Welding Symposium, Chicoutimi, QC, Canada, 26–28 June 2018.